

Th_P01_07

3D Elastic FWI with a Non-Linear Model Constraint: Application to a Real Complex Onshore Dataset

P. Trinh^{1*}, R. Brossier², L. Lemaistre¹, L. Métivier^{2,3}, J. Virieux²

¹ TOTAL E&P; ² Univ. Grenoble Alpes, ISTerre; ³ Univ. Grenoble Alpes, CNRS, LJK

Summary

Full waveform inversion (FWI) of 3D onshore targets is very challenging due to the complex free-surface-related and heterogeneities effects. In such areas, the seismic wavefield displays converted and back-scattering energy, with a strong contribution of surface waves. A time-domain spectral-element-based approach is used for accurate elastic wavefield simulation in mountain areas. The challenges of the elastic multi-parameter FWI in complex land areas are highlighted through a real foothill dataset. Various practical issues such as a significant amount of noise in the data, sparse acquisition and topography representation uncertainty must be considered. We illustrate how additional prior information such as well logs and geological knowledge can be used to assist the FWI workflow. First, a non-linear model constraint on the ratio V_p/V_s , relying on the logs information, may better constrain the V_s based on the stable V_p estimation. Second, appropriate gradient preconditioning design is also crucial for meaningful model parameters reconstruction. At the current stage, the inversion mainly focuses on the early-body waves, which are gradually incorporated through a progressive time-windowing. The strategy helps to mitigate the cycle-skipping issue at the later arrivals and maximize the considering data quantity, and eventually improve the model estimation.

Introduction

Full waveform inversion (FWI) for onshore targets is very challenging due to complex free-surface-related effects and 3D geometry representation. In such areas, the seismic wavefield is dominated by highly energetic and dispersive surface waves, converted waves and back-scattering energy when the waves hit the steep slopes at the surface, or strong velocity contrasts. These complex effects cannot be fully removed or compensated by data pre-processing, implying that a correct description of the physics is strongly advisable for accurate model parameters estimation. Moreover, considering the complete physical phenomena of the wave propagation would make possible to take benefit of each piece of recorded data, for expected more accurate results and higher resolution. Adequate geometry representation is also required to honor the interaction between elastic waves and geological structures such as rapid topography variation and erosions. When considering complex structures or geological heterogeneities, regularization and preconditioning strategies also play an important role to mitigate the ill-posedness of the inversion problem (Guitton et al., 2012; Trinh et al., 2017).

Our previous studies have demonstrated the possibility to recover simultaneously V_p and V_s from various synthetic benchmarks (Trinh et al., 2018, 2019). In this study, we investigate a 3D multi-parameter elastic FWI workflow on a 2D real seismic line, acquired from a complex foothill area with significant topography variation. The sub-surface is characterized by complex faulting, significant folding and highly dipping structures. The rough topography variation and the excessive amount of noises make the standard velocity model building approach very difficult, for instance velocity picking and tomography techniques. The work is performed using our SEM46 code (Spectral Element Method for Seismic Imaging in eXploration), based on a time-domain spectral element method (SEM) (Trinh et al., 2019).

Wave propagation and FWI in SEM46

The code uses a flexible Cartesian-based deformed mesh with high-order geometry representation to capture complex topographies and variable element-size to reduce the numerical cost as illustrated in Figure 1 (Trinh et al., 2019). The wavefield at the boundary is absorbed by a combination of sponge layers and radiative boundary condition (Trinh, 2018). The inversion is based on the minimization of the least-squares norm between the observed and the calculated data. The FWI gradient preconditioning is directly performed on the SEM mesh, by using the structurally-based nonstationary and anisotropic Bessel smoothing filter (Trinh et al., 2017). The filter shape is defined by variable coherence lengths: $L_v(\mathbf{x})$ is associated with the direction perpendicular to the local bedding plan, $L_u(\mathbf{x})$ and $L_w(\mathbf{x})$ are related to the planar structure of potential geological features. The 3D orientation is controlled by azimuth and dip angles.

Non-linear model constraint on the ratio V_p/V_s

Elastic FWI applications with the least-squares misfit function is generally more sensitive to V_s . When considering significant geological heterogeneities, the inversion process might lead to *unrealistic updates* where $V_s > V_p$ or too small value of V_s . Therefore, additional prior information should be incorporated in addition to the standard gradient smoothing strategy to further guide the inversion process.

We introduce a non-linear constraint on the ratio V_p/V_s , which is applied simultaneously with the bound constraints on the range of V_p and V_s . The misfit function is now minimized over a restricted model space ($\mathcal{C}_1 \cap \mathcal{C}_2$), which is the intersection of two convex sets:

- Bound constraint \mathcal{C}_1 : V_p and V_s should vary within pre-defined ranges,
- Ratio constraint \mathcal{C}_2 : The ratio V_p/V_s should vary within a pre-defined range.

These constraints can be designed based on well logs or simple geological knowledge about the structure. The projection of model parameters onto the intersection of two constraints are performed through the Dykstra's algorithm, which ensures the uniqueness of the solution, independently with the order of the constraints application (Peters and Herrmann, 2017; Trinh, 2018).

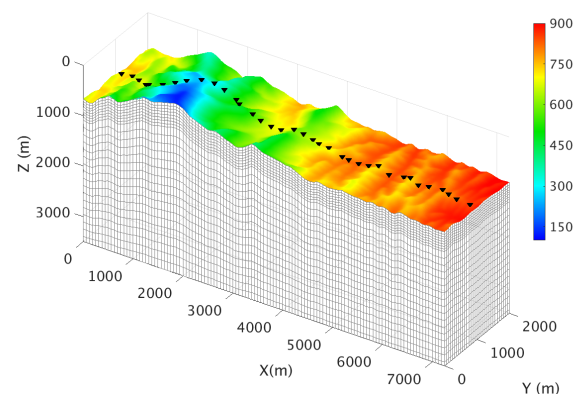
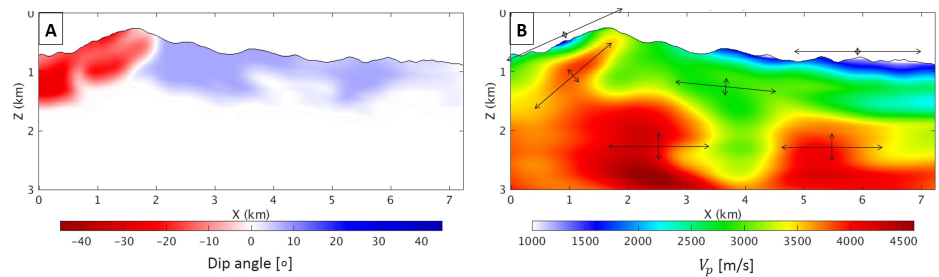


Figure 1 The 3D SEM mesh designed at 4 Hz maximal frequency: 62.5 m elements size at the near surface and 175 m elements size at the deeper part. The topography map is put on top of the mesh, where the colorbar illustrates the absolute depth $Z_{abs}(m)$ from a pre-defined datum. The source positions of the 2D line are indicated by black triangles ($\Delta S = 200$ m).

Figure 2 Gradient preconditioning design: A - The dip field: The first 1 km below the free-surface is extracted from the initial V_p ; B - The cartoon to illustrate the effect of the smoothing operator onto the gradient.



Foothill dataset configuration

The considered 2D line is located across the mountain trend with significant topography change as shown in Figure 1. We limit the investigated area at 7.2 km in the x -direction. The entire seismic line is acquired with explosive sources, buried at 7 m depth. This source type produces un-controlled source signature but it also generates the low frequency content, down to 2 Hz, which is beneficial for FWI. All receivers are single vertical (z) component, located at the free-surface. The sources and receivers follow the same line, as indicated by the black triangles in Figure 1. The acquisition has significant deviation in the y direction, at about 400 m, especially when crossing the mountain. This deviation implies that the 3D effect consideration is advisable for any imaging technique. The source and receiver spacings are not regular with rather sparse distribution: the average distance between adjacent receivers is approximately 37 m, and about 40 m between adjacent sources.

Inversion setup

Since our SEM46 tool can perform true-amplitude and waveform elastic waves propagation, we do not apply any sophisticated processing sequences such as static correction or surface waves removal. We only remove the low frequency noises below 2 Hz by a high-pass filter. The data within the range [2-4 Hz] is considered for inversion, which provides a reasonable signal to noise ratio.

Initial models & Mesh design

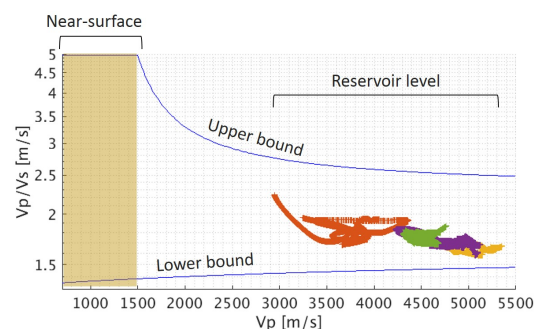
The initial V_p model is provided by the data owner as shown in Figure 4A. The initial V_s and density models are computed from the given V_p through some empirical relationships, obtained from upscaling logs data. The initial models quality control shows acceptable starting data fit for the selected frequency range. To account for the 3D propagation effect, we consider a narrow 3D model with 2 km in y -direction. Due to the limitation of 7.2 km offset in x -direction, we do not expect any model update below 3.5 km in depth. Since we expect significant heterogeneities at the near-surface, the first 500 m in z -direction is filled with small elements. The element sizes are computed from the expected shear wavelength. The mesh design for the maximal frequency at 4 Hz is shown in Figure 1. Each element is deformed by 4th-order shape functions to describe the sharp topography (Trinh et al., 2019).

Gradient preconditioning and model constraints

To prepare for any rapid vertical velocity variation at the near-surface, the preconditioning has highly anisotropic shape at this area with vertical coherence length being $L_v = 16$ m, and horizontal coherence lengths as $L_u = 200$ m. It should be noted that L_v is equivalent to a quarter of the element size at the near-surface (62.5 m as shown in Figure 1) and a large value of L_u is used to attenuate the acquisition footprint due the sparse source spacing. In the deeper part with bigger element size, we use larger coherence lengths with $L_v = 70$ m and $L_u = 150$ m.

The highly anisotropic smoothing at the near-surface requires an “appropriate” rotation design, otherwise the preconditioning operator might introduce thin pinch-out artifacts following unexpected direction. The initial models provides rather good velocity trends, correctly following the topography and the expected

Figure 3 The design of model constraint on the ratio V_p/V_s based on wells data. A tight constraint on the ratio V_p/V_s is considered at the reservoir level normally associated with large V_p value, whereas a less strict constraint is applied at the near-surface.



structures orientation for the first 1 km. We thus compute the near-surface dip field from the initial V_p and the deeper part is set to 0° as shown in Figure 2A. The filtering orientation is illustrated in Figure 2B. When inverting simultaneously for V_p and V_s , we suffer from the instability of the V_s reconstruction meanwhile the V_p remains stable. This comes from the lack of shear information in the explosive seismic data. At each spatial position \mathbf{x} , we thus constraint the estimated $V_s(\mathbf{x})$ through the inverted $V_p(\mathbf{x})$ following the non-stationary constraint on the ratio $V_p/V_s(\mathbf{x})$. A tight constraint on this ratio is considered at the reservoir level, normally associated with large V_p value, whereas a less strict constraint is applied at the near-surface as shown in Figure 3. The upper and lower bounds are computed from V_p (Trinh, 2018).

Inversion workflow

At this stage, we only consider the early body waves packages, arriving before the surface waves. The challenging incorporation of surface waves is under investigation. A simple bottom mute is used to separate the early body waves and surface waves. In the body waves packages, the cycle-skipping issue occurs for the later arrivals but not for the early arrivals. We thus design a progressive time-window to incorporate gradually the later arrivals into the inversion process. Each time-window is defined by a pair of top and bottom mutes, designed from the first-break, given by the data owner. The top mute is important to remove the coherent noises arriving before the first arrival. The bottom mute increases progressively by a half of the apparent wavelength per time-window.

The inversion contains different sequences, each being performed over one time-window with 4 iterations of the preconditioned l -BFGS optimization method. Within each sequence, the density and the source wavelet are kept unchanged. Since a relative short data interval with few traces is considered as the FWI input, we keep relatively small number of iterations per sequence. After each inversion sequence, the source wavelet is re-estimated, and the density is computed from the obtained V_p model.

Inversion results & Discussion

The inversion process makes some significant amplitude changes in both V_p and V_s models as shown in Figure 4B. The main fault trend which already existed in the initial model is preserved in the inverted models. The trend is further refined in the inverted V_p , and the high V_p value is propagated up to the free-surface, which is coherent with the geological observation. The inversion also remove all the low- V_p values at the near-surface, and considerably increases the V_p background.

The inverted V_s is more difficult to interpreted since it has a considerable amount of artifacts. This is due to the fact that the early body waves, acquired by the explosive sources, bring limited shear information. Even if the main fault direction is presented, the dimming of the estimated V_s at the top of the mountain, at $X \approx 1.8$ km, is not coherent with the high velocity trend in V_p . The inverted V_s detects some interesting low velocity trends at the near-surface, indicated by the black arrows in Figure 4. Their coherent appearance, size and amplitude in various FWI setting make us believe that they are geologically correct. The geological interpretation of the area indeed shows some possible near-surface ruptures. Since the available logs data are not located along the seismic line, they cannot be used to control the quality of inverted models.

An about 100 m thickness low-velocity layers underneath the free-surface appears in the V_s model, as indicated by the red arrow in Figure 4B. This low-velocity layer does not have coherent shape and has never been detected by the V_p estimation through our various FWI settings. Its appearance is not supported by any geological evidence. This inconsistency makes us believe that it is not geological correct.

Figure 5 shows the comparison of the maximal 4 Hz real data with the calculated computed from initial

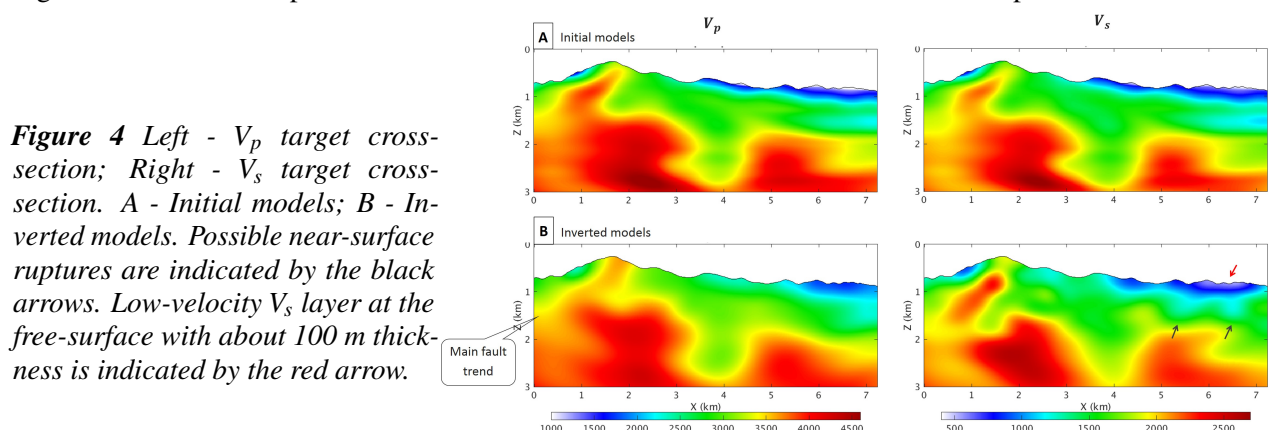


Figure 4 Left - V_p target cross-section; Right - V_s target cross-section. A - Initial models; B - Inverted models. Possible near-surface ruptures are indicated by the black arrows. Low-velocity V_s layer at the free-surface with about 100 m thickness is indicated by the red arrow.

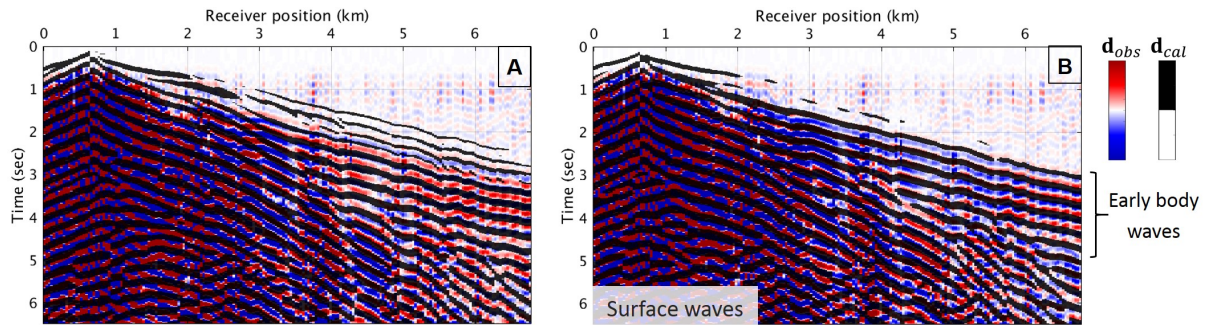


Figure 5 Data comparison for the first shot between the observed data \mathbf{d}_{obs} and calculated data \mathbf{d}_{cal} : (A) \mathbf{d}_{cal} estimated from initial models in Figure 4A, (B) \mathbf{d}_{cal} estimated from inverted models in Figure 4B. Observed data is displayed with red-and-blue color. Calculated data is displayed with black and transparent color. Good data-fit is identified when the red loops are perfectly covered by the black loops.

models and inverted models in Figure 4. Compared with the real data, the initial models produce relatively good wavefield prediction, with coherent body and surface waves. However, the early body waves package is cycle-skipped, apart from some first arrivals (Figure 5A). By injecting real data progressively through the progressive time-widows strategy, we improve the early body waves fitting as indicated by Figure 5B. We seem to also have a better surface waves prediction and mode conversion, for example at around 3 km position. However, the predicted data is almost cycle-skipped at the far offsets, at 6 km position. This issue is also detected in other shot gathers which further confirms the 100 m near-surface anomaly in V_s in Figure 4B. We have investigated these near-surface artifacts by a synthetic feasibility study. It seems that such artifacts are caused by the acquisition mis-positioning in depth, coming from the surface elevation measurement error: The source depth available in the data SEG Y header (GPS information) and the LIDAR topography maps are not totally consistent.

Conclusions and perspectives

The presented application illustrates the challenges in a real foothill environments. Apart from the data complexity and elastic multi-parameter FWI problem, we have to deal with various practical issues such as a significant amount of noise in the data, sparse acquisition and topography representation uncertainty. We illustrate how additional prior information such as well logs and geological knowledge can be used to assist the FWI workflow. A V_p -dependent non-linear model constraint on the ratio V_p/V_s , relying on the logs information, is considered to constrain the V_s based on the stable V_p estimation. In the next steps, we plan to consider more shots to compensate for the data lacking, also to investigate on alternative misfits design to better handle the cycle-skipping issue. However, a carefully re-processed data at might help to improve the inverted models quality.

Acknowledgements

This study was partially funded by TOTAL and the SEISCOPE consortium (<http://seiscope2.osug.fr>), sponsored by AKERBP, CGG, CHEVRON, EQUINOR, EXXON-MOBIL, JGI, PETROBRAS, SCHLUMBERGER, SHELL, SINOPEC and TOTAL. This study was granted access to the HPC resources of CIMENT infrastructure (<https://ciment.ujf-grenoble.fr>) and CINES/IDRIS/TGCC under the allocation 046091 made by GENCI. We thank TOTAL for providing the HPC resources and permission to present this work.

References

- Guittou, A., Ayeni, G. and Díaz, E. [2012] Constrained full-waveform inversion by model reparameterization. *Geophysics*, **77**(2), R117–R127.
- Peters, B. and Herrmann, F.J. [2017] Constraints versus penalties for edge-preserving full-waveform inversion. *The Leading Edge*, **36**(1), 94–100.
- Trinh, P.T. [2018] *3D Multi-parameters Full Waveform Inversion for challenging land targets*. Ph.D. thesis, University Grenoble Alpes.
- Trinh, P.T., Brossier, R., Métivier, L., Tavad, L. and Virieux, J. [2019] Efficient 3D time-domain elastic and viscoelastic Full Waveform Inversion using a spectral-element method on flexible Cartesian-based mesh. *Geophysics*, **84**(1), R75–R97.
- Trinh, P.T., Brossier, R., Métivier, L. and Virieux, J. [2018] Data-oriented strategy and V_p/V_s model-constraint for simultaneous V_p and V_s reconstruction in 3D viscoelastic FWI: Application to the SEAM II Foothills dataset. In: *88th SEG Conference and Exhibition 2018, Anaheim*.
- Trinh, P.T., Brossier, R., Métivier, L., Virieux, J. and Wellington, P. [2017] Bessel smoothing filter for spectral element mesh. *Geophysical Journal International*, **209**(3), 1489–1512.